The Astrophysical Journal, 622:830–841, 2005 April 1

THE HALO, HOT SPOTS, AND JET/CLOUD INTERACTION OF PKS 2153−69

A. J. Young,[1] A. S. Wilson,[2,3] S. J. Tingay,[4] and S. Heinz[1,5]

Received 2004 July 22; accepted 2004 November 1

ABSTRACT

We report *Chandra X-Ray Observatory* and 1.4 GHz Australian Long Baseline Array (LBA) observations of the radio galaxy PKS 2153−69 and its environment. The *Chandra* image reveals a roughly spherical halo of hot gas extending out to 30 kpc around PKS 2153−69. Two depressions in the surface brightness of the X-ray halo correspond to the large-scale radio lobes, and interpreting these as cavities inflated with radio plasma, we infer a jet power of 4×10^{42} ergs s^{-1}. Both radio lobes contain hot spots that are detected by *Chandra*. In addition, the southern hot spot is detected in the 1.4 GHz LBA observation, providing the highest linear resolution image of a radio lobe hot spot to date. The northern hot spot was not detected in the LBA observation. The radio to X-ray spectra of the hot spots are consistent with a simple power-law emission model. The nucleus has an X-ray spectrum typical of a type 1 active galactic nucleus, and the LBA observation shows a one-sided nuclear jet on $0\farcs1$ scales. Approximately $10''$ northeast of the nucleus, X-ray emission is associated with an extranuclear cloud. The X-ray emission from the cloud can be divided into two regions, an unresolved western component associated with a knot of radio emission (in a low-resolution map), and a spatially extended eastern component aligned with the parsec-scale jet and associated with highly ionized optical line–emitting clouds. The X-ray spectrum of the eastern component is very soft ($\Gamma > 4.0$ for a power-law model, or $kT \simeq 0.22$ keV for a thermal plasma). The LBA observation did not detect compact radio emission from the extranuclear cloud. We discuss both jet precession and jet deflection models to account for the progressively increasing position angle from the northern hot spot to the western component of the jet/cloud interaction region to the direction of the parsec-scale jet. In the precession model the particle beam impacts the western region, while the radiation beamed from the nucleus photoionizes the eastern region and is scattered into our line of sight by dust, giving rise to the polarized optical emission and possibly the soft X-ray emission. If the X-ray emission from the eastern region really is dust-scattered nuclear radiation, it would be the first detection of such emission from an external galaxy. The nearby galaxy MRC 2153−699 is also detected by *Chandra*.

Subject headings: cosmic rays — galaxies: active — galaxies: individual (PKS 2153−69) — galaxies: jets — magnetic fields — X-rays: galaxies

1. INTRODUCTION

The morphology of a typical radio galaxy is strongly influenced by interactions between the relativistic jet that originates at its nucleus and material in the interstellar and intergalactic media. This appears true at all stages of radio galaxy evolution. In the GHz peaked spectrum and compact steep spectrum objects, in many cases thought to be radio galaxies in the early stages of evolution (Snellen et al. 2003), interactions between their jets and their nuclear environment have been observed (e.g., O'Dea et al. 2002). In the more mature, low-power FR I type radio galaxies, entrainment of material by a relativistic jet has been suggested as the mechanism responsible for their expanding, decelerating jets and center-brightened radio lobes (e.g., Bicknell 1994). In contrast, in the higher power FR II radio galaxies, interactions between the jets and the intergalactic medium terminate the jets in spectacular lobe hot spots, giving these radio galaxies their characteristic edge-brightened large-scale morphologies (i.e., Carilli et al. 1991; Perley et al. 1997).

The jets themselves and the interaction regions produce emission via both thermal and nonthermal mechanisms over a wide range of spatial scales, from subparsec to megaparsec. Much of the detailed physics pertaining to relativistic jets in radio galaxies is still uncertain (De Young 2005), and the complexity of the physics involved in interactions between these jets and their environments is underscored by a number of recent theoretical and numerical simulation studies (e.g., Hughes et al. 2002).

With these considerations in mind, it is immediately apparent that high spatial resolution, multiwavelength observations of radio galaxies are a prerequisite for detailed investigations of the physical processes involved. The benefits of high spatial resolution, multiwavelength observational studies of radio galaxies are illustrated by recent work on the nearby radio galaxies Pictor A (Wilson et al. 2001; Perley et al. 1997) and Centaurus A (Hardcastle et al. 2003).

PKS 2153−69 is one of the few nearby and powerful radio galaxies, a transition FR I/FR II object (Fosbury et al. 1998) at a redshift of $z = 0.0282$ (Tadhunter et al. 1988). The proximity of PKS 2153−69 (20% closer than Pictor A) makes it an ideal object in which to study a relativistic jet and its relationship to its environment. As well as the strong radio lobe hot spots typical of FR II radio galaxies, PKS 2153−69 also contains one of the best examples of an interaction between a relativistic jet and an extranuclear cloud of gas (Tadhunter et al. 1987, 1988; Fosbury et al. 1998, 1990; di Serego Alighieri et al. 1988). Radio and optical imaging by Fosbury et al. (1998) and VLBI observations by Tingay et al. (1996) have provided good evidence that a jet

[1] MIT Center for Space Research, 77 Massachusetts Avenue, Cambridge, MA 02139.
[2] Astronomy Department, University of Maryland, College Park, MD 20742.
[3] Adjunct Astronomer, Space Telescope Science Institute, 3700 San Martin Drive, Baltimore, MD 21218.
[4] Centre for Astrophysics and Supercomputing, Swinburne University of Technology, Mail No. 31, P.O. Box 218, Hawthorn, Victoria 3122, Australia.
[5] Chandra fellow.

originating at the nucleus of the host galaxy impacts a cloud of gas in the outskirts of the galaxy, possibly the remnant of a merging galaxy. Near the interaction site, an optically emitting cloud (line and continuum) with a complex morphology and ionization structure is seen.

In this paper we present observations that address the twin goals of multiwavelength coverage and improved spatial resolution. First, comprehensive *Chandra* X-ray–imaging observations of PKS 2153−69 are presented, including analyses of the major X-ray–emitting regions of the system: the hot halo, the nucleus, the jet/cloud interaction, and the lobe hot spots. Second, high spatial resolution radio observations (VLBI) are presented that are targeted to the aforementioned regions of interest. In particular, we present the highest linear resolution observation of a radio galaxy lobe hot spot yet produced.

We attempt to produce a coherent physical picture of the jet interaction regions in this radio galaxy by considering the *Chandra* X-ray data, VLBI data, archival *Hubble Space Telescope* (*HST*) data, and other published data.

We use the *Wilkinson Microwave Anisotropy Probe* measured cosmology of $H_0 = 71$ km s^{-1} Mpc^{-1} and $\Omega_\Lambda = 0.73$ (Bennett et al. 2003). PKS 2153−69 has a redshift of $z = 0.0282$, which corresponds to a luminosity distance of 123 Mpc and $1'' = 566$ pc. The Galactic column density toward PKS 2153−69 is $N_{\rm H} = 2.5 \times 10^{20}$ cm^{-2} (Dickey & Lockman 1990).

2. OBSERVATIONS

2.1. *X-Ray*

PKS 2153−69 was observed by the *Chandra X-Ray Observatory* on 2001 August 2 for 14 ks. The nucleus was placed at the aim point of the ACIS-S detector, and CCDs 2, 3, 5, 6, 7, and 8 were active, in the standard full-frame mode with a frame time of 3.2 s. The observation was mildly affected by background flares that increased the background count rate to approximately 4/3 of the quiescent rate. Since most of the X-ray–emitting regions are small, we chose not to remove the periods of high background since this would significantly degrade the signal-to-noise ratio. Data were extracted using CIAO 3.0.2 with CALDB 2.26, and analyzed using XSPEC 11.3.0. The degradation of the low-energy response of ACIS due to molecular contamination is taken into account using the latest CIAO tools. The *Chandra* astrometry is excellent, and the position of the X-ray nucleus differs from the position of the radio nucleus quoted by Fosbury et al. (1998) by only 0.″2. When overlaying the radio maps of Fosbury et al. (1998) on our *Chandra* images, we have aligned the brightest pixel in the radio map with the brightest pixel in the *Chandra* image.

2.2. *Radio*

PKS 2153−69 was observed with three elements of the Australian Long Baseline Array (LBA) on 2003 February 15: the 22 m Mopra Telescope, three of the six 22 m antennas of the Australia Telescope Compact Array (ATCA) tied together as a phased array, and the 64 m Parkes Telescope. The observation was conducted over a 6 hr period, and the data were recorded using the S2 system (Wietfeldt et al. 1996), consisting of dual polarization 16 MHz bands centered at 1400 MHz. Each 16 MHz band was 2 bit sampled, giving an aggregate recorded data rate of 128 Mbps.

The recorded data were shipped to the LBA correlator (Wilson et al. 1996) and correlated using a 5 s integration time and 32 frequency channels across each 16 MHz band. The cross polarization products were not correlated. The synthesized beam, using uniform weighting, gives a restoring beam for imaging of approximately 90 mas × 150 mas at a position angle of −67°.

Once correlated, system temperatures and antenna gains were applied to the data in AIPS,[6] to calibrate the visibility amplitudes. Adjustments to the calibration were derived from a short observation of a strong unresolved source (PKS B1921−293) and applied to the PKS 2153−69 data. The data were then fringe-fitted in AIPS, each polarization independently. The residual delays and rates were applied to the data before the data were exported to disk. The data were not averaged in time or frequency, and all 32 of the 0.5 MHz frequency channels were retained and multifrequency synthesis techniques are used in the imaging process.

The strong and compact source at the nucleus of the radio galaxy (the phase tracking center used at the correlator) was imaged in DIFMAP (Shepherd 1997), following editing of the data and averaging in time over a 10 s timescale. With only three antennas in the array, only phase self-calibration was possible.

The self-calibrated data following imaging of the nuclear radio source were imported into the MIRIAD processing software (Sault et al. 1995). In MIRIAD, a model of the nuclear source was produced in the (u, v)-plane and was subtracted from the data. Then the data were edited so that the phase-tracking center was shifted, entailing an appropriate recalculation of (u, v) coordinates. Three shifted data sets were produced in this way. The first of the shifted data sets placed the phase-tracking center on the brightest part of the southern lobe of the radio galaxy (the southern lobe hot spot). The second shifted data set placed the phase-tracking center at the northern lobe hot spot. Finally, the third shifted data set was centered at the location that marks the point of interaction between the northern jet and a cloud of gas in the host galaxy. The coordinates of these three new phase-tracking centers were estimated from the published ATCA images of Fosbury et al. (1998). In this way, images of these three regions could be formed by Fourier inversion and deconvolution.

2.3. *Archived Hubble Space Telescope Image*

An *HST* F606W image of PKS 2153−69 was obtained from the *HST* archive. This is the same image as presented in the optical/radio comparison of PKS 2153−69 in Fosbury et al. (1998). The *HST* image was initially cleaned of cosmic rays using the Figaro task *bclean*. The coordinate system of the *HST* image was then shifted to align the brightest pixel ($\alpha = 21^{\rm h}57^{\rm m}06^{\rm s}.248$, $\delta = -69°41'23''.79$ [J2000.0]) with the brightest radio and X-ray pixels ($\alpha = 21^{\rm h}57^{\rm m}06^{\rm s}.038$, $\delta = -69°41'23''.78$ [J2000.0]).

3. MORPHOLOGY

3.1. *Hot Halo and Radio Lobes*

The large-scale 0.5–7 keV X-ray and 4.7 GHz radio morphologies of PKS 2153−69 are shown in Figure 1. The radio map shows two lobes, each of which contains a hot spot. The X-ray image shows a halo of hot gas extending out to a radius comparable to that of the radio lobes, approximately $1' = 30$ kpc. There are depressions in the X-ray surface brightness at the location of the radio lobes suggesting that the radio plasma has

[6] The Astronomical Image Processing Software (AIPS) has been developed and is maintained by the National Radio Astronomy Observatory, which is operated by Associated Universities, Inc., under cooperative agreement with the National Science Foundation.

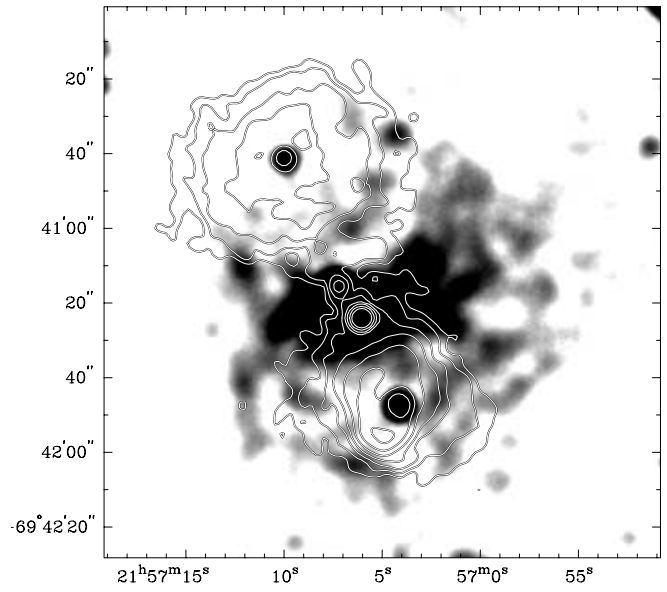

FIG. 1.—*Chandra* X-ray image in the 0.5–7 keV band, with contours of an ATCA 4.7 GHz radio map (Fosbury et al. 1998) overlaid. Here and throughout the paper, coordinates are J2000.0 epoch. The *Chandra* image has been smoothed by a Gaussian of FWHM 6″, and the radio map has been smoothed by a Gaussian of FWHM 3″. A diffuse halo of hot gas is seen in the X-ray image, extending out to a radius comparable to that of the radio lobes. There are depressions in the X-ray surface brightness at the locations of the radio lobes. Each radio lobe contains a radio and X-ray hot spot.

inflated cavities in the intergalactic medium. The southern cavity is completely embedded in the halo gas, but the northern cavity appears to have "broken out" of the halo to the northeast and may be less well confined by the halo gas. A higher resolution X-ray image is shown in Figure 2, and the highlighted regions are discussed below.

3.2. *Nucleus*

The VLBI observation (Fig. 3) shows that the nuclear radio source consists of a strong unresolved component (the core) and

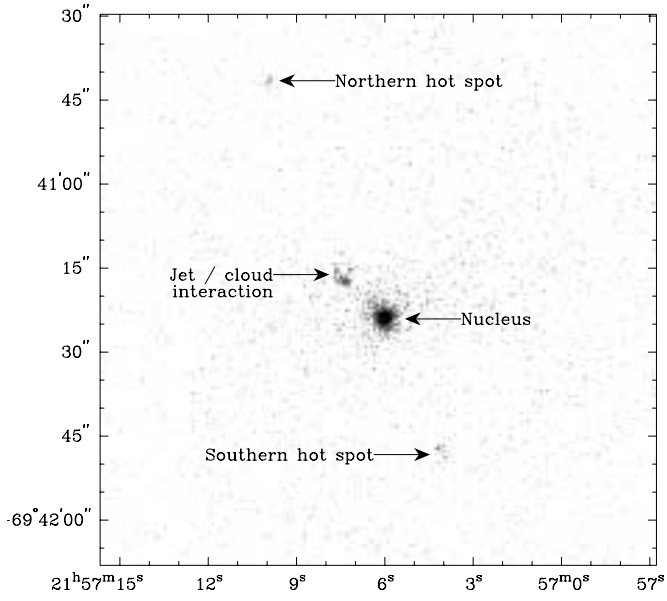

FIG. 2.—Full-resolution *Chandra* X-ray image in the 0.5–7 keV band with interesting regions labeled.

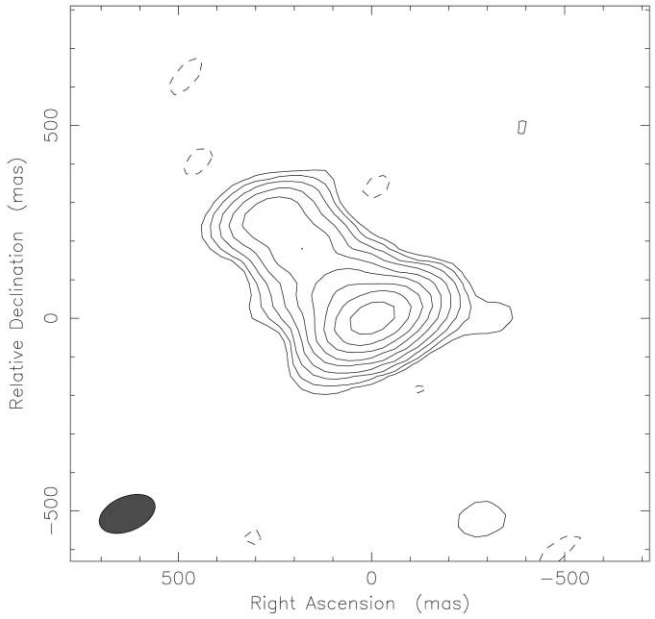

FIG. 3.—A 1.4 GHz VLBI image of the radio nucleus of PKS 2153−69, as described in the text. Contours are −0.25%, 0.25%, 0.5%, 1%, 2%, 4%, 8%, 16%, 32%, and 64% of the peak, 0.379 Jy beam^{-1}. The restoring beam size is 152 mas $\times$90 mas at a major axis position angle of −67°.

a weaker extension along a position angle (P.A.) of ∼45° (the jet). Assuming the jet is continuous and has a spectral index of $\alpha = 0.7$ ($S \propto \nu^{-\alpha}$), the flux ratio between the jet and counter jet is

$$R = [(1 + \beta_j \cos\theta)/(1 - \beta_j \cos\theta)]^{2+\alpha} > 8.1, \qquad (1)$$

from which we derive

$$\beta_j \cos\theta > 0.37 \qquad (2)$$

for the parsec-scale jet, where $\beta_j = v_j/c$ is the velocity of the material in the jet and θ the angle between the jet and the line of sight.

The X-ray nucleus is also spatially extended toward the northeast on a much larger scale (Fig. 4). A more quantitative description of the X-ray morphology of the nucleus is difficult because the ACIS image suffers from pile-up, having an observed count rate of 0.17 counts s^{-1}.

3.3. *Jet/Cloud Interaction Region*

Approximately 10″ northeast of the nucleus there are a series of clouds that lie roughly along the position angle of the VLBI jet. The X-ray emission from the clouds can be divided into two regions (Fig. 4). First, centered at a nuclear distance of 9.″0 along a P.A. of 45° there is a region of X-ray emission that is spatially resolved, with an extent of ≃4.″5 along the jet direction and an extent of ≃2.″5 transverse to the jet direction. We shall refer to this region as the eastern component of the jet/cloud interaction region. Second, at a nuclear distance of 10.″6 along a P.A. of 34° (Fig. 4) there is a compact source of X-ray emission. We shall refer to this region as the western component of the jet/cloud interaction region. To test whether the western region is resolved by *Chandra* we consider the counts within a 0.″5 radius circle and a surrounding annulus of inner radius 0.″5 and outer radius 2.″5. The region of the annulus that overlaps the eastern component is excluded, and the counts in the remainder of the annulus are

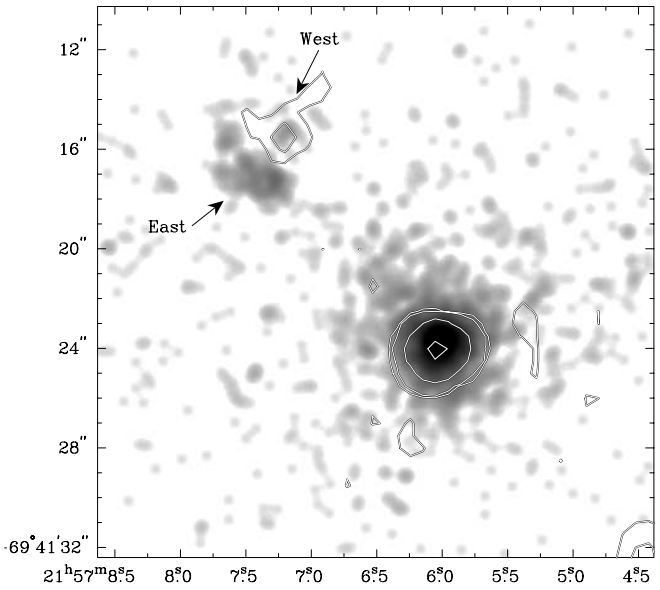

FIG. 4.—*Chandra* 0.5–7 keV X-ray image of the nucleus and jet/cloud interaction region of PKS 2153−69 with contours of an ATCA 8.6 GHz radio map (Fosbury et al. 1998) overlaid. The *Chandra* image has been resampled to 10 times smaller pixel size and smoothed by a Gaussian of FWHM 0.″5. The X-ray emission from the jet/cloud interaction region approximately 10″ northeast of the nucleus can be divided into two regions, a spatially extended eastern region (labeled "east") and an unresolved western region (labeled "west"). The western region is associated with a knot of radio emission.

scaled to account for the lost area. The background count rate due to the diffuse halo is estimated from a region at a similar nuclear distance to the east of the nucleus. We find that 75% of the counts above the diffuse background level come from within $\lesssim$0.″5 of the western region. This is comparable to that expected for a soft X-ray point source ($\simeq$80%), so the western component is consistent with being an unresolved point source superposed on diffuse halo emission. An optical image of the nucleus and jet/cloud interaction region taken with *HST* is shown in Figure 5, with contours of *Chandra* X-ray emission and VLBI 1.4 GHz radio emission overlaid. The *HST* image (Fig. 5; Fosbury et al. 1998) shows optical emission from a number of filamentary clouds in the region associated with the X-ray emission. Ground-based optical spectra of these filaments show emission lines from a range of very highly ionized ions, including strong [Fe x] λ6375 (Tadhunter et al. 1987, 1988; di Serego Alighieri et al. 1988; Fosbury et al. 1990, 1998). Fosbury et al. (1998) detect radio emission from the western component associated with the unresolved X-ray emission (Fig. 4). Our VLBI observation did not detect any radio emission from the jet/cloud interaction region with a 3 σ upper limit of 3 mJy beam^{-1}.

3.4. *Southern Hot Spot*

At a nuclear distance of 25″ along a P.A. of 202° (Fig. 6) X-ray emission is seen to approximately coincide with the radio emission from the southern hot spot, although there is a tentative suggestion that the peak of the X-ray emission is slightly closer to the nucleus than the peak of the radio emission (the offset is only $\simeq$0.″5 $\simeq$1 *Chandra* pixel and is at the limit of *Chandra*'s astrometric accuracy). The VLBI observation detected significant emission from the southern lobe hot spot (Fig. 7). The compact

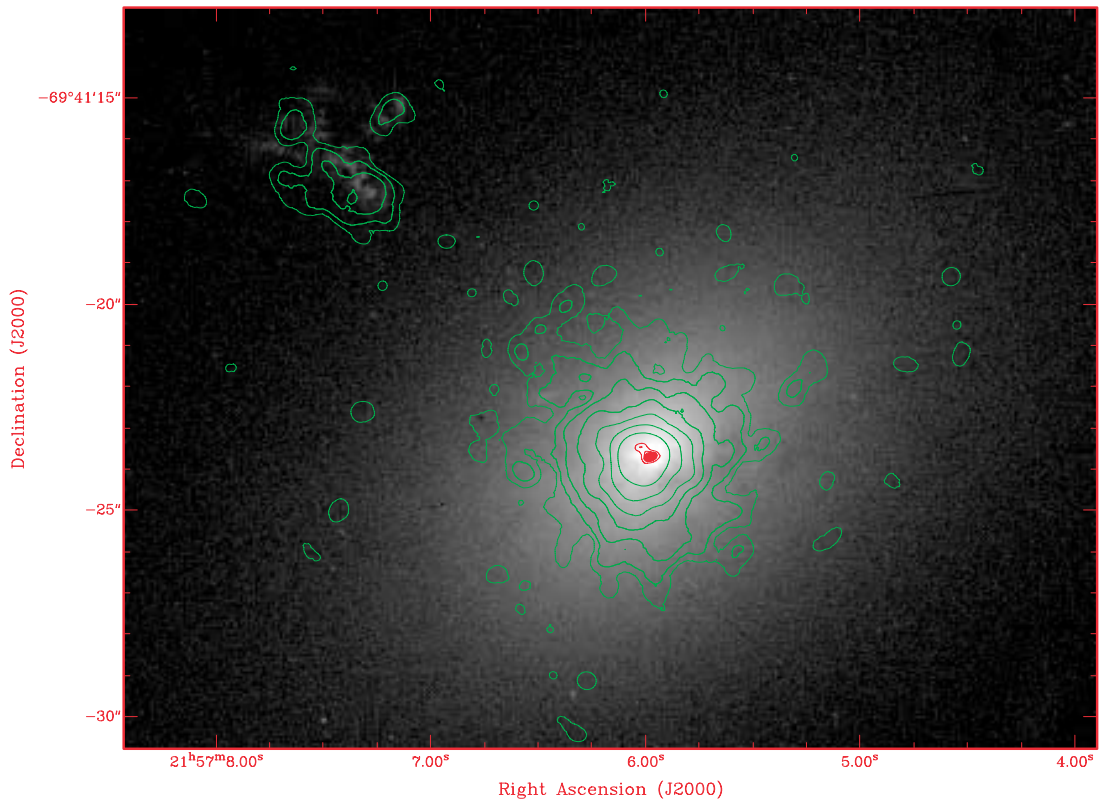

FIG. 5.—*HST* F606W image of the PKS 2153−69 host galaxy (*gray scale*) with *Chandra* X-ray contours (*green*) overlaid. Also, 1.4 GHz radio contours for the nuclear radio source (*red*) are overlaid.

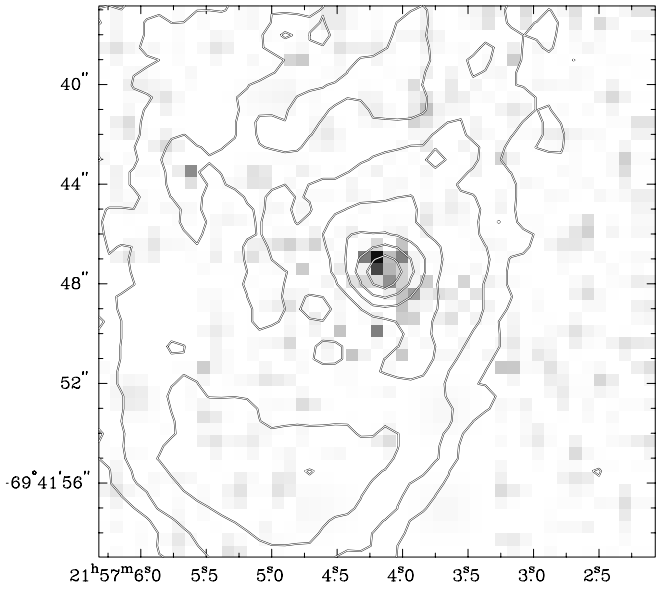

FIG. 6.—*Chandra* 0.5–7 keV X-ray image of the southern hot spot with contours of an 8.6 GHz radio map (Fosbury et al. 1998) overlaid.

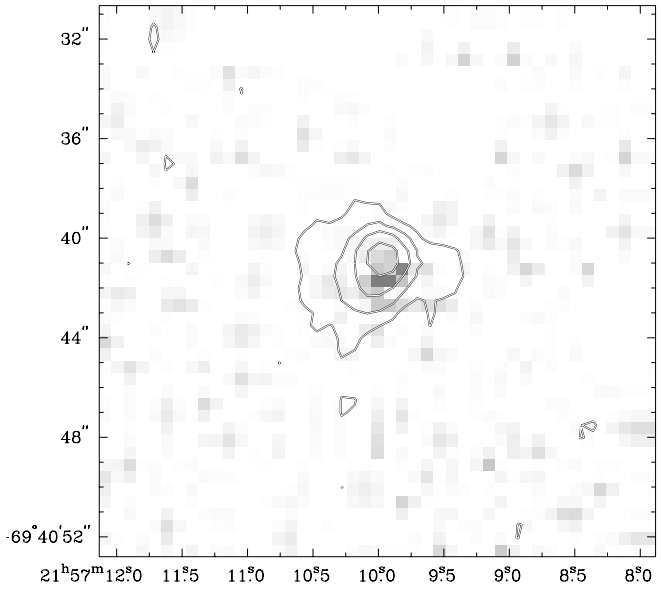

FIG. 8.—*Chandra* 0.5–7 keV X-ray image of the northern hot spot with contours of an 8.6 GHz radio map (Fosbury et al. 1998) overlaid.

radio emission at the southern lobe hot spot can be adequately represented in the image plane by three circular Gaussian components, separated by approximately 400 mas, one component with a FWHM of 140 mas and a total flux density of 35 mJy, the second component with a FWHM of 220 mas and a total flux density of 65 mJy, and the third component with a FWHM of 100 mas and a total flux density of 10 mJy. The VLBI image of the southern lobe hot spot shown in Figure 7 is the highest linear resolution image of a radio galaxy lobe hot spot ever produced, to the best of our knowledge. Previously, Perley et al. (1997) imaged the western hot spot of Pictor A with the VLA at a wavelength of 2 cm, giving a best angular resolution of 90 mas. The best angular resolution of Figure 7 is also 90 mas (at a wavelength of 20 cm, however), giving a linear resolution approximately 20% better than the Pictor A hot spot since PKS 2153−69 is approximately 20% closer than Pictor A.

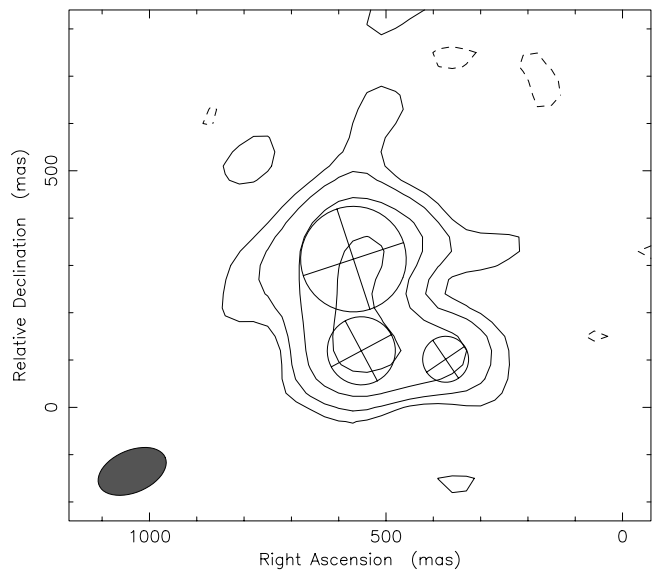

FIG. 7.—1.4 GHz VLBI image of the southern lobe hot spot of PKS 2153−69, as described in the text. Contours are −10%, 10%, 20%, 40%, and 80% of the peak, 17.2 mJy beam^{-1}. The restoring beam size is 152×90 mas at a major axis position angle of $-67°$. The circles represent the FWHM of the three circular Gaussian components used to model the structure of the radio source (the crosses inside the circles have arbitrary position angles).

3.5. *Northern Hot Spot*

At a nuclear distance of 47″ along a P.A. of 26° (Fig. 8), faint X-ray emission is seen to approximately coincide with the radio emission from the northern hot spot, although there is a tentative suggestion that the peak of the X-ray emission is slightly closer to the nucleus than the peak of the radio emission, as was the case for the southern hot spot (and also at the limit of *Chandra*'s astrometric accuracy). Our VLBI observation did not detect any radio emission from this region with a 3 σ upper limit of 3 mJy beam^{-1}. If we assume that the northern lobe hot spot has a similar size and structure as the southern lobe hot spot, we estimate that an upper limit to the total flux density of the compact emission from the northern lobe hot spot is approximately 25 mJy.

4. X-RAY SPECTRA

The extraction regions for the sources and backgrounds are given in Table 1. Any emission that is unrelated to the region of interest was excluded.

4.1. *Hot Halo*

The spectrum is well described by a MEKAL (Mewe et al. 1985, 1986; Kaastra 1992; Liedahl et al. 1995) thermal plasma model with a temperature of $kT = 1.01$ keV (see Table 2). The metallicity is significantly subsolar, with $Z = 0.28\ Z_{\odot}$.

4.2. *Nucleus*

The nuclear spectrum suffers from the effects of pileup, which are corrected using the routine of Davis (2001) that is available in XSPEC (Arnaud 1996). The spectrum is well described by a power-law model with photon index $\Gamma = 1.75$ and a 2–10 keV luminosity of 8.7×10^{42} ergs s^{-1} absorbed by the Galactic column (see Table 2). This is typical of a "type 1" active galaxy or quasar.

TABLE 1
EXTRACTION REGIONS FOR SPECTRA

Region	Aperture for Source[a]	Radius/Radii of Source Aperture	Range of P.A. for Source Aperture (deg)	Aperture for Background[a]	Radius/Radii of Background Aperture	Range of P.A. for Background Aperture (deg)
Halo (§ 4.1)	Circle[b]	1.′1	All	Annulus[c]	1.′1 (inner), 1.′8 (outer)	All
Nucleus (§ 4.2)	Circle	4.″4	All	Annulus	4.″4 (inner), 7.″9 (outer)	All
Jet/cloud interaction region (§ 4.3):						
Eastern	Annulus[d]	7.″4 (inner), 13.″3 (outer)	41–60	Annulus[d]	7.″4 (inner), 13.″3 (outer)	60–26
Western	Annulus[e]	7.″4 (inner), 13.″3 (outer)	26–41	Annulus[e]	7.″4 (inner), 13.″3 (outer)	60–26

[a] All apertures are centered on the nucleus.
[b] Nuclues, jet/cloud interaction region and hot spots omitted.
[c] Two bright point sources omitted.
[d] Does not include the unresolved western component of the jet/cloud interaction region.
[e] Does not include the eastern component of the jet/cloud interaction region.

4.3. *Jet/Cloud Interaction Region*

If the spectrum of the extended eastern component is modeled as a power law absorbed by the Galactic column, we find that the spectrum is very soft with $\Gamma > 4.0$, although this gives a poor fit with a χ^2/dof (degrees of freedom) of 10.5/6. A thermal plasma of solar abundance absorbed by the Galactic column provides a slightly better description of the spectrum with $kT = 0.22$ keV and a χ^2/dof of 9.8/6. The poor χ^2 value of the thermal plasma model is a result of the spectrum being slightly harder than the model, with excess flux around 1.5 keV (there are too few counts to model the spectrum above ~2 keV). An excellent description of the spectrum is obtained if a power law of photon index $\Gamma = 1$ is added to the thermal plasma model, giving a χ^2/dof of 3.5/5 (see Table 2 and Fig. 9). The power-law component accounts for approximately 18% of the unabsorbed 0.5–2 keV flux. We do not have a sufficient signal-to-noise ratio to strongly constrain this hard component, but a power law of photon index $\Gamma = 1$ is equivalent to a very hot bremsstrahlung component. Thus, an equally good description of the spectrum is obtained by replacing the power-law component with a second, high-temperature thermal plasma ($kT > 3.9$ keV). Attempting to model the spectrum as a sum of two power-law components absorbed by the Galactic column gives an unacceptable χ^2/dof of 10.5/4 with significant systematic residuals below 0.8 keV where the thermal plasma model has strong iron L shell emission lines. We conclude that the X-ray emission from the extended eastern component of the jet/cloud interaction region may originate from a thermal plasma with $kT = 0.22$ keV, with a weaker high-temperature or nonthermal component. An alternative interpretation, discussed in § 5.4, is that the X-rays from this eastern component are dust-scattered radiation of a blazar X-ray beam from the nucleus. This beam would be directed at the eastern part of the cloud. However, we continue here our discussion of the thermal plasma interpretation.

Assuming the eastern component arises from shock heating of a cold gas cloud, we can estimate the shock velocity. The Rankine-Hugoniot shock jump conditions (Landau & Lifshitz 1959) give a shock velocity v_s of

$$v_s^2 = \frac{16kT}{3\mu m_{\rm H}}, \tag{3}$$

where $\mu = 0.61$ is the mean mass per particle in units of the proton mass, and we have assumed a fully ionized gas and solar abundances. For a postshock temperature of $kT = 0.22$ keV we estimate a shock velocity of $v_s \simeq 430$ km s^{-1}.

The unresolved western component of the jet/cloud interaction region is too faint to obtain its X-ray spectrum directly, but we can form a hardness ratio R based on the number of counts S in a soft band (0.5–1.2 keV) and the number of counts H in a hard band (1.2–5 keV), given by $R = (H - S)/(H + S)$. We find $R = -0.13^{+0.23}_{-0.22}$. If we assume the spectrum is a power law absorbed by the Galactic column this corresponds to $\Gamma = 2.1^{+0.5}_{-0.5}$. The error bars on R and Γ quoted here (and in subsequent sections dealing with hardness ratios) denote the 90% confidence interval assuming independent Poisson statistics for S and H. If

TABLE 2
X-RAY SPECTRAL MODELS

Region	Model	Parameter	Normalization[a]	Unabsorbed Flux (ergs s^{-1}) 0.5–2 keV	Unabsorbed Flux (ergs s^{-1}) 2–10 keV	Unabsorbed Luminosity (ergs s^{-1}) 0.5–2 keV	Unabsorbed Luminosity (ergs s^{-1}) 2–10 keV	χ^2/dof
Halo	MEKAL	$kT = 1.01^{+0.06}_{-0.06}$ keV	$5.4^{+1.3}_{-0.9} \times 10^{-4}$	3.9×10^{-13}	...	6.8×10^{41}	...	...
	Metallicity	$Z = 0.28^{+0.10}_{-0.09}\ Z_\odot$	...	...	...	...	...	44.4/60
Nucleus	Power law	$\Gamma = 1.75^{+0.08}_{-0.05}$	$1.4^{+0.1}_{-0.7} \times 10^{-3}$	3.0×10^{-12}	5.0×10^{-12}	5.1×10^{42}	8.7×10^{42}	117.7/129
Jet/cloud (east)	MEKAL	$kT = 0.22^{+0.02}_{-0.03}$ keV	$2.5^{+0.7}_{-0.5} \times 10^{-5}$	3.4×10^{-14}	...	6.2×10^{40}	...	...
	MEKAL plus power law	$\Gamma = 1.0$[b]	$2.6^{+0.8}_{-1.6} \times 10^{-6}$	6.1×10^{-15}	...	1.0×10^{40}	...	3.5/5

NOTE.—All models include absorption by only the Galactic column. The error bars indicate the 90% confidence interval for a single interesting parameter ($\Delta\chi^2 = 2.7$).
[a] The power-law normalization is photons cm^{-2} s^{-1} keV^{-1} at 1 keV. The MEKAL thermal plasma model normalization is $10^{-14} \int n_e n_{\rm H}\, dV / \{4\pi[D_A(1+z)]^2\}$ where D_A is the angular size distance (cm), and n_e and $n_{\rm H}$ are the electron and hydrogen densities (cm^{-3}), respectively.
[b] Parameter fixed.

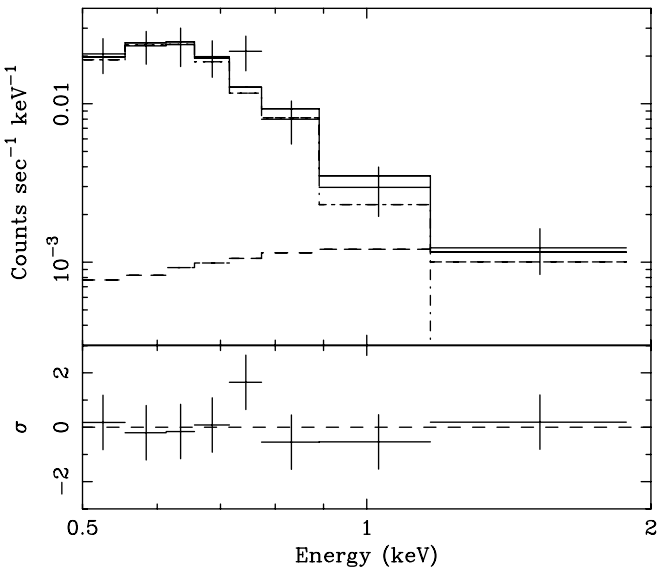

FIG. 9.—*Chandra* X-ray spectrum of the eastern component of the jet/cloud interaction region. The top panel shows the spectrum (*plus signs*) with the best-fit model overlaid (*solid line*). The model consists of a thermal plasma component (*dot-dashed line*) and a hard power-law component (*dashed line*). The bottom panel shows the χ residuals to the model. See § 4.3 and Table 2 for details.

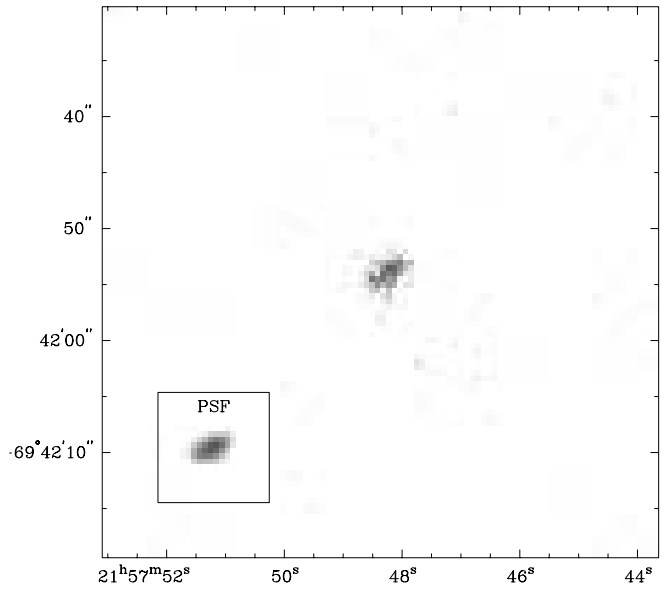

FIG. 10.—*Chandra* 0.5–7 keV X-ray image of the radio galaxy MRC 2153−699 that lies almost 4′ to the east of PKS 2153−69. The off-axis point-spread function (PSF) of *Chandra* is shown in the inset panel, and the nucleus is not clearly resolved.

the spectrum is a power law of photon index $\Gamma = 2.1$ absorbed by the Galactic column, the flux density is 2.3×10^{-32} ergs cm^{-2} s^{-1} Hz^{-1} at 1 keV (see Table 3). If, on the other hand, the spectrum is a thermal plasma, this hardness ratio corresponds to a temperature of $kT = 2.5^{+3.8}_{-1.0}$ keV, with the same flux density.

4.4. *Northern and Southern Hot Spots*

Neither hot spot has sufficient counts to obtain an X-ray spectrum. We can, however, determine their hardness ratios using the technique and hard and soft bands described in § 4.3. We find that the northern hot spot has $R = -0.16^{+0.29}_{-0.25}$, which, for a power-law model absorbed by the Galactic column, corresponds to $\Gamma = 2.2^{+0.6}_{-0.7}$. The flux density at 1 keV assuming such a spectrum is 1.4×10^{-32} ergs cm^{-2} s^{-1} Hz^{-1} (see Table 3). Similarly, we find that the southern hot spot has $R = -0.19^{+0.25}_{-0.21}$, which, for a power-law model absorbed by the Galactic column, corresponds to $\Gamma = 2.2^{+0.6}_{-0.5}$. The flux density assuming such a spectrum is 1.9×10^{-32} ergs cm^{-2}s^{-1} Hz^{-1} (see Table 3).

4.5. *The Nearby Galaxy MRC 2153−699*

We also detect X-ray emission from the nucleus of the radio galaxy MRC 2153−699 that lies almost 4′ to the east of PKS 2153−69 (Fig. 10). The spectrum of MRC 2153−699 is reasonably well described (χ^2/dof = 10/8) by an absorbed ($N_{\rm H} = 1.1^{+1.0}_{-1.0} \times 10^{22}$ cm^{-2}) power law ($\Gamma = 0.9^{+0.7}_{-0.4}$) with an observed 1–5 keV X-ray flux of 1.9×10^{-13} ergs cm^{-2} s^{-1}. Its redshift and therefore luminosity are unknown, although it has been identified with a 20th magnitude galaxy (Jones & McAdam 1992) and imaged in the radio by Fosbury et al. (1998).

TABLE 3
X-RAY FLUX DENSITIES

Region	$\log_{10}$(Frequency) (Hz)	$\log_{10}$(Flux Density) (ergs cm^{-2} s^{-1} Hz^{-1})
Jet/cloud (west).....	17.4	−31.6
Northern hot spot.....	17.4	−31.9
Southern hot spot.....	17.4	−31.7

5. DISCUSSION

5.1. *Hot Halo*

The hot halo has a radius of approximately 1′, a temperature of $T \simeq 10^7$ K, an electron number density of $n_e \simeq 7 \times 10^{-3}$ cm^{-3}, and a pressure $P \simeq 10^{-11}$ dyn cm^{-2}. The electron density is calculated using the emission measure of the X-ray thermal plasma model and assuming the halo is a uniform density spherical cloud. The total mass of halo gas is $M_{\rm gas} \simeq 3 \times 1010\, M_\odot$, which is probably only a small fraction of the gravitating mass in the halo. If we assume that the depressions in the X-ray–emitting halo corresponding to the radio lobes are cavities filled with relativistic radio plasma, we can estimate the power of the jet. The sound speed in the halo is $c_s \simeq 3 \times 10^7$ cm s^{-1}. The southern lobe has a radius of ≃15.″5, and the southern hot spot is 25″ from the nucleus. Using the sound crossing time, $t_{\rm sc}$, from the nucleus to the southern hot spot as a characteristic timescale, we estimate the jet power required to inflate the southern cavity to be $F_j \simeq 4PV_{\rm cavity}/t_{\rm sc} = 2 \times 10^{42}$ ergs s^{-1}, where $V_{\rm cavity}$ is the volume of the cavity. Since there are two cavities the total jet power is $F_j \simeq 4 \times 10^{42}$ ergs s^{-1}, which is a factor of ∼3 below the X-ray luminosity of the nucleus (in the 0.5–10 keV band).

5.2. *Northern and Southern Hot Spots*

The spectral energy distribution of the northern hot spot is shown in Figure 11. The northern lobe hot spot was not detected in our VLBI observation with an estimated upper limit to the total flux density of the compact emission of approximately 25 mJy (see § 3.5). The more diffuse 4.7 GHz radio emission associated with the northern hot spot has a flux density of 210 mJy and a spectral slope of $\alpha = 0.87$ (the spectral indices measured from the lower resolution radio maps should be interpreted with caution because the observations were not made with matched arrays; Fosbury et al. 1998). A power-law model provides a good description of the spectrum, although if the emitting region is

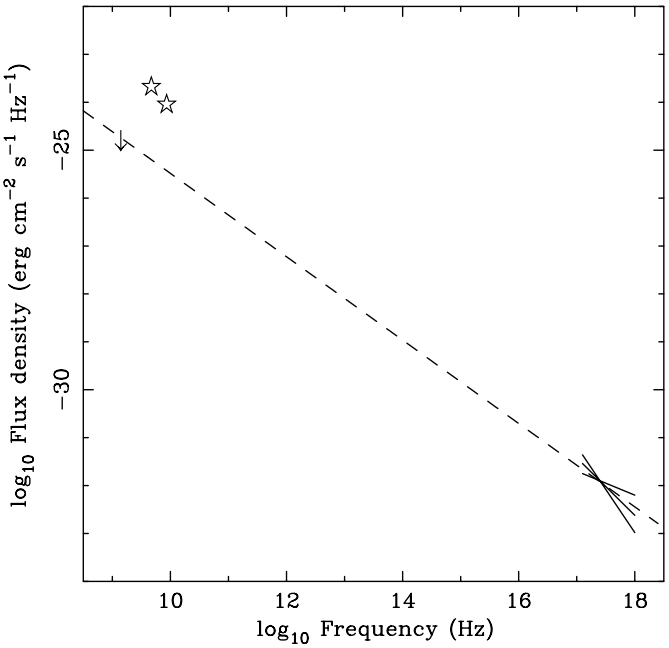

FIG. 11.—Spectral energy distribution of the northern hot spot showing the 1.4 GHz radio flux of the compact source (upper limit), the 4.7 GHz and 8.6 GHz fluxes of the more extended emission (*stars*), and the X-ray spectrum (*bow tie*). The dashed line shows a power law $S_\nu \propto \nu^{-0.87}$ (the more diffuse radio emission associated with the northern hot spot was estimated to have a spectral slope of 0.87 by Fosbury et al. 1998).

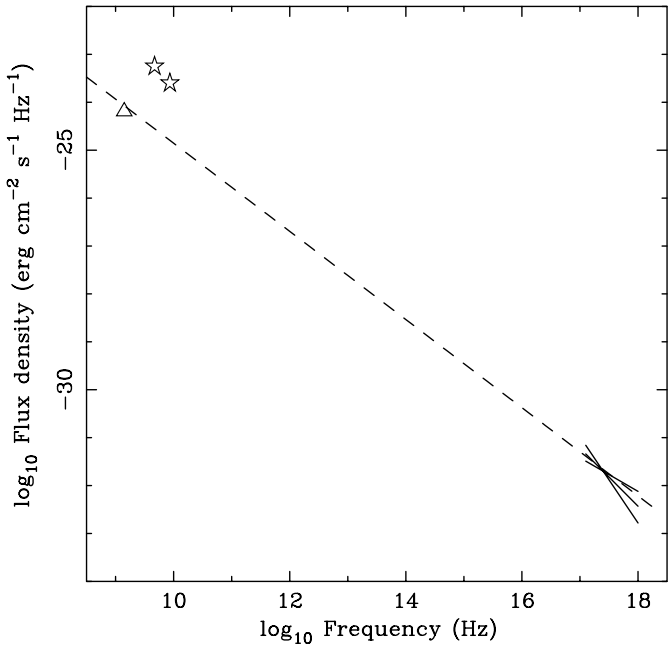

FIG. 12.—Spectral energy distribution of the southern hot spot showing the 1.4 GHz radio flux of the brightest compact knot (*triangle*), the 4.7 GHz and 8.6 GHz fluxes of the more extended emission (*stars*), and the X-ray spectrum (*bow tie*). The dashed line shows a power law $S_\nu \propto \nu^{-0.92}$ (the more diffuse radio emission associated with the southern hot spot was estimated to have a spectral slope of 0.92 by Fosbury et al. 1998).

spatially unresolved, its 1.4 GHz radio flux density should be just below the upper limit.

The spectral energy distribution of the southern hot spot is shown in Figure 12. The 1.4 GHz flux density of the brightest knot in our VLBI image of the southern hot spot is 65 mJy, which is significantly lower than the 4.7 GHz flux density of 560 mJy reported by Fosbury et al. (1998). This difference in flux densities is just due to the significant difference in beam sizes. If the X-ray emission is associated with the compact knots in the VLBI image, we find that a power-law model provides an excellent description of the spectrum, with a spectral slope of $\alpha = 0.92$ that is equal to the radio spectral slope estimated by Fosbury et al. (1998). The 1.4 GHz radio to X-ray spectral slope is $\alpha_{rX} = 0.94$.

5.3. *The Jet/Cloud Interaction*

As shown in Figures 4 and 5, the jet/cloud interaction region in PKS 2153−69 has a complex multiwavelength structure. The eastern component of the region (Figs. 4 and 5) consists of an ensemble of highly ionized filamentary clouds, with the highest ionization clouds closest to the nucleus (Tadhunter et al. 1988). Spectra of these clouds also reveal the presence of a blue polarized continuum that may be scattered light from the active nucleus (Villar-Martín et al. 2001; Fosbury et al. 1998). In § 4.3 we concluded that the X-rays observed from the eastern component may come from a thermal plasma with $kT = 0.22$ keV, plus some additional weaker high-temperature or nonthermal emission. An alternative, discussed in § 5.4, is that the X-rays, like the optical continuum, are light from the "blazar" nucleus that has been scattered by dust into our line of sight. The VLBI jet (§ 3.2) is seen to be highly aligned with the set of clouds that make up the eastern component (Tingay et al. 1996, 2002).

The western component of the interaction region (Fig. 5) is dominated by a feature that has a red optical continuum, in contrast to the blue continuum of the eastern component. Radio emission has been observed coincident with the western component by Fosbury et al. (1998), and here we have reported the detection of X-ray emission (§ 4.3), although it is unclear whether this emission is thermal or nonthermal in nature. The position angle connecting the nucleus and the western component is approximately 10° less than the position angle of the VLBI jet direction that intersects the center of the eastern component (Fosbury et al. 1998).

Confronted with these facts, can we plausibly identify the region within the ensemble of clouds where the primary jet interaction occurs?

For a start, it appears unlikely that the radio jet has an opening angle that encompasses the entire cloud complex, both the eastern and western components. The opening angle of the nuclear jet, from VLBI Space Observatory Program observations, is very small, less than a few degrees (Tingay et al. 2002). Also, the diameter of the jet at the southern lobe hot spot is presumably less than the measured diameter of the hot spot itself, approximately 200 pc. Therefore, it is likely that the primary site of interaction will be confined to only a small part of the cloud complex. It is likely that many shocks exist within the cloud complex as a result of the jet interaction (Bicknell et al. 1998), and it may be these secondary shocks that are powering the thermal X-ray emission throughout the region.

Previously, it has been suggested that the red continuum of the western component is radiation from a foreground star (di Serego Alighieri et al. 1988). However, the existence of both radio and X-ray emission coincident with this component almost certainly marks it as integral to the cloud complex. Villar-Martín et al. (2001) give an alternative explanation for the red continuum: they suggest that it results from large dust grains scattering red light from the active nucleus, the small dust grains in this component having been destroyed by shocks in a jet/cloud interaction. According to this explanation, the blue continuum of the eastern component is a result of scattering of

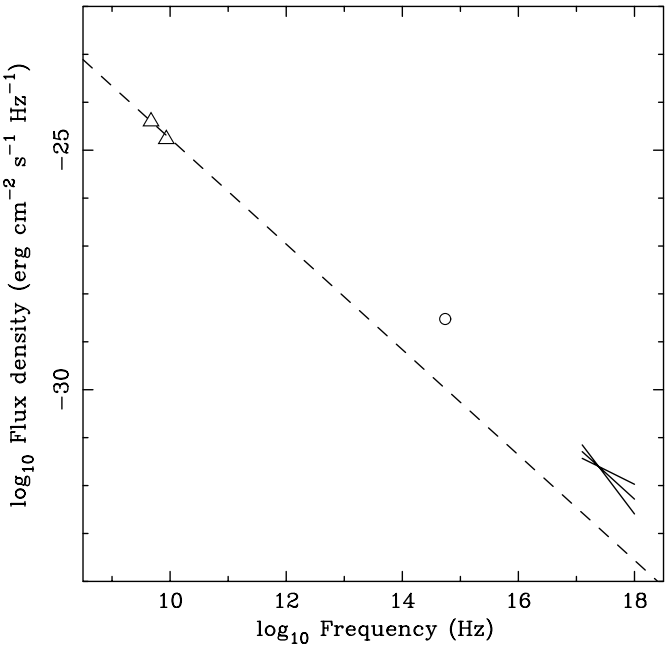

FIG. 13.—Spectral energy distribution of the western component of the jet/cloud interaction region from radio (*triangles*) through optical (*circle*) to X-ray (*bow tie*) wavelengths. The dashed line shows a power-law spectrum $S_\nu \propto \nu^{-\alpha}$ with $\alpha = 1.1$ corresponding to the estimated spectral slope of the radio emission (Fosbury et al. 1998). The radio flux densities are taken from Fosbury et al. (1998) and the western component was not detected in our VLBI observation. The optical flux density is from di Serego Alighieri et al. (1988).

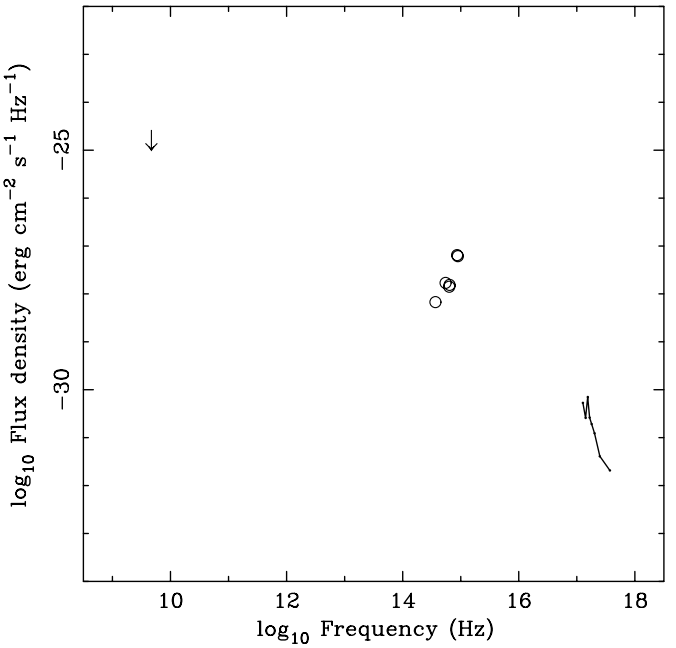

FIG. 14.—Spectral energy distribution of the eastern component of the jet/cloud interaction region from radio (*upper limit*) through optical (*circles*) to X-ray (*solid line*) wavelengths. The radio upper limit was estimated from Fosbury et al. (1998), and the optical continuum flux densities (which follow a ν^{+3} law) are from di Serego Alighieri et al. (1988). The X-ray spectrum shows the data unfolded using the best-fit model given in Table 2. The optical continuum emission is ≃12% linearly polarized (di Serego Alighieri et al. 1988) and is probably radiation that has been beamed from the nucleus and scattered into our line of sight by dust in the cloud. The X-ray emission may be similarly dust-scattered nuclear light or thermal plasma emission.

blue light from the nucleus by small dust grains that are preserved because the eastern component is not as heavily shocked as the western component. Identification of the western component as the primary jet interaction site, via this argument, is consistent with the presence of radio synchrotron emission (increased synchrotron emissivity due to enhanced electron energy and compressed magnetic field in the shocked region) and X-ray emission. Figure 13 shows the radio to X-ray spectrum for the western component. This spectrum could be plausibly fitted with a power law with the spectral slope given by Fosbury et al. (1998) and an additional optical component of red light from the nucleus scattered by large dust grains (Villar-Martín et al. 2001). There is also thermal X-ray emission from a hot plasma (see § 4.3). The scattered optical and thermal X-ray emission dominate and are at least an order of magnitude stronger than the synchrotron emission extrapolated to optical and X-ray wavelengths.

However, there is a problem with identifying the western component as the primary jet interaction site. All VLBI imaging observations of the nuclear radio jet show that it is highly aligned with the eastern component, not the western component. Further, the strongest X-ray emission from the cloud complex comes from the eastern component. The radio to X-ray spectrum of the eastern component is shown in Figure 14. A solution to this problem might be that radiation beamed from the nucleus along the VLBI jet direction is being scattered by dust into our line of sight giving rise to the observed optical and X-ray emission. We consider this possibility below.

5.4. *Dust Scattering*

The eastern component of the jet/cloud interaction region is illuminated by radiation beamed along the VLBI jet direction from the nucleus, and some of this radiation may be scattered by dust into our line of sight. The polarized, blue optical continuum is thought to be the result of dust scattering (Villar-Martín et al. 2001), and it is possible that the X-ray emission is also the result of dust scattering. If the radiation beamed from the nucleus has a BL Lac spectrum, the ratio of the optical to X-ray flux densities seen by the cloud will be approximately $L_{\nu,\mathrm{opt}}/L_{\nu,\mathrm{X}} = 2\times10^2$ to 2×10^3 (Fossati et al. 1998). The differential scattering cross section for blue light is $(d\sigma/d\Omega)_{\mathrm{opt}} \simeq 2\times10^{-22}$ cm^2 sr^{-1} H^{-1} (Draine 2003) for $\theta_s \lesssim 20^\circ$, where H^{-1} denotes per hydrogen nucleon. Here we have averaged the results for the Milky Way and the LMC plotted in Figure 3 of Draine (2003). The differential scattering cross section for 0.45 keV X-rays is $(d\sigma/d\Omega)_{0.45\ \mathrm{keV}} \simeq 1.5\times10^{-20}(\theta_s/1^\circ)^{-3}$ cm^2 sr^{-1} H^{-1} for $\theta_s \gtrsim 0.^\circ3$, where θ_s is the scattering angle and the -3 exponent has been estimated from Figure 8 of Draine & Tan (2003). These scattering cross sections assume a Milky Way distribution of dust grain sizes and composition. The observed ratio of the optical to X-ray flux density of the eastern component is approximately $F_{\nu,\mathrm{opt}}/F_{\nu,\mathrm{X}} = 10^3$, and this constrains the scattering angle since

$$\frac{F_{\nu,\mathrm{opt}}}{F_{\nu,\mathrm{X}}} \simeq \frac{L_{\nu,\mathrm{opt}}}{L_{\nu,\mathrm{X}}}\frac{(d\sigma/d\Omega)_{\mathrm{opt}}}{(d\sigma/d\Omega)_{\mathrm{X}}} \simeq 1000\left(\frac{L_{\nu,\mathrm{opt}}/L_{\nu,\mathrm{X}}}{2\times10^2}\right)\left(\frac{\theta_s}{6^\circ}\right)^3, \quad (4)$$

giving $\theta_s = 3^\circ$–6° for $L_{\nu,\mathrm{opt}}/L_{\nu,\mathrm{X}} = 2\times10^2$ to 2×10^3, respectively. Given the uncertainties in the spectral energy distribution of the radiation beamed from the nucleus, the distribution of dust grain sizes, and the scattering angle, it may be that the X-ray emission from the eastern component represents dust scattering of nuclear light. However, the predicted X-ray intensity is only comparable to that observed if θ_s is only a few degrees, and there is no evidence that the radio axis of PKS 2153−69 is at such a small angle to the line of sight. If the X-rays *are* dust-scattered,

this cloud in PKS 2153−69 would be the first example of this process in an extragalactic context.

5.5. *Electron Scattering*

Radiation beamed from the nucleus toward the eastern component of the jet/cloud interaction region may be electron scattered into our line of sight as long as the scattering medium is highly ionized, so that soft X-ray absorption is negligible and has a sufficiently large column density. We consider electron scattering to be unlikely, however, because the spectrum of the eastern region of the jet/cloud interaction region ($\Gamma > 4$) is much softer and clearly not the same as the spectrum of the nucleus ($\Gamma = 1.75$). The cloud complex might see a much softer spectrum than we do, which is possible if soft X-rays from the nucleus are heavily obscured in our direction but propagate freely to the scattering cloud. The X-ray spectrum of the nucleus, however, does not show additional absorption in excess of the Galactic column, so it is unlikely that there is such an obscured soft X-ray source in the nucleus.

5.6. *Jet Precession*

A solution to the problem of having two different sites of interaction within the cloud (one for the radiation beam and one for the particle beam) is jet precession. If the jet is slow ($v_j \ll c$) and the jet precesses across the cloud complex, a time delay between the photon beam from the nucleus and the particle beam reaching a given part of the cloud complex will exist. Such a scenario may explain the fact that the western component has radio, optical, and X-ray emission consistent with a jet/cloud interaction region, while the eastern component has a high degree of ionization (photoionization from the beamed nuclear radiation, plus a possible contribution from any secondary shocks in the cloud due to the interaction in the western component) and scattered nuclear continuum light.

For this hypothesis to be viable, the jet precession rate must be slow enough that, at present, the direction of the nuclear jet (which is presumed to align with the nuclear photon beam and hence with the photoionized eastern component of the cloud complex) is only 15°–20° in projection from the direction between the nucleus and the western component of the cloud complex, where the jet's interaction with the cloud is presumed to take place. The light-travel time between the nucleus and the cloud complex is approximately $20,000/\sin\theta$ yr (θ is the angle between the jet and our line of sight). During this time the nuclear jet can only have changed its true orientation by less than a few degrees (the angular extent of the eastern cloud as seen from the nucleus), in order to remain in near alignment with the eastern component, giving a rate of change for the jet orientation of $<2\times10^{-4}\sin\theta$ deg yr^{-1}. Thus, at this rate of change, the jet material that is currently impacting the western component of the cloud system was ejected from the nucleus at least $40{,}000/\sin\theta$ yr ago. The inferred speed of the jet is therefore $<0.5c$ (averaged over the journey from the nucleus to the cloud system). The jet speed inferred from equation (2) is higher than this for some values of θ, but at its origin in the nucleus the jet may well be faster than it is several kiloparsecs away at the clouds, because of deceleration.

Also the sense of the jet precession (from western to eastern component), if mirrored on the opposite side of the nucleus, follows a curved feature evident in the radio emission that ends at the current terminus of the southern jet in an active lobe hot spot (as seen from the VLBI images). Alternatively, this curved feature in the southern lobe could be interpreted as backflow from the lobe hot spot. The jet precession hypothesis predicts that the current nuclear counterjet (not visible because of beaming effects; see eq. [2]) should not align with the southern lobe hot spot but should be pointed somewhat to the west of the hot spot. If we assume that the nuclear counterjet is diametrically opposed to the observed nuclear jet (which is likely given that this is the case for every counterjet yet observed), then the ATCA images of Fosbury et al. (1998) agree with the prediction. The counterjet position angle would then be approximately 19° greater than the position angle joining the nucleus and the southern lobe hot spot (Fosbury et al. 1998). At a jet speed of $0.5c$, this 19° offset represents a jet orientation rate of change very close to that estimated for the northern jet at the cloud complex, and in the same sense. The P.A. of the northern hot spot with respect to the nucleus is lower than the P.A. of the jet/cloud interaction site (the western component), giving an overall "S-shape" to the radio source.

We can extend this argument to the position of the northern hot spot, taking into account the finite jet speed, light-travel time, and projection effects. Our model consists of symmetric back-to-back ballistic jets moving at constant speed v_j and precessing at a rate Ω with the precessing jet direction forming a cone of half-opening angle θ_c. The symmetry axis of the cone is inclined at an angle i to our line of sight. The radio lobes are approximated by spheroids, and the hot spots are assumed to lie on the surfaces of the spheroids. An additional parameter is the present day azimuthal phase of the jet ϕ. Given an inclination i and a cone half-opening angle θ_c, we can solve for Ω, v_j, and ϕ from trigonometric and light-travel time considerations. For all possible values of i and θ_c we compare the predicted jet path with the observed hot spot positions and pick solutions that have the smallest deviation. There is not a unique solution for i and θ_c, so we choose the one with the largest v_j given the VLBI beaming constraints. These precession solutions for both possible values of ϕ and both positive and negative Ω are shown in Figure 15. In this model $i = 40\overset{\circ}{.}5$, $\theta_c = 11\overset{\circ}{.}6$, $\beta_j = v_j/c \simeq 0.3$, and the current inclination angle of the parsec-scale jet to our line of sight is $\simeq 40°$. Two solutions have precession rates of $\Omega \simeq -2\times10^{-4}$ deg yr^{-1}, and two have $\Omega \simeq 5\times10^{-4}$ deg yr^{-1}, where positive Ω implies precession in a clockwise sense. The slower precession rates give the "straighter" curves in Figure 15 and are in good agreement with the precession rates expected from the jet orientation rates of change estimated above and the geometry adopted for the precession model.

5.7. *Jet Deflection*

The idea of jet precession, as outlined in the previous section, seems to plausibly explain a great many of the observed features of PKS 2153−69 at X-ray, radio, and optical wavelengths. Previously, Tingay (1997) suggested that the radio morphology of PKS 2153−69 is affected by the deflection of the northern jet at the site of the jet/cloud interaction, causing the observed difference between the nuclear jet position angle and the position angle joining the nucleus and the northern lobe hot spot. For the reasons stated above, we feel that jet precession gives a better overall explanation of the multiwavelength source structure, but we briefly revisit the alternative jet deflection explanation, using the previously unavailable constraints from the X-ray observations.

Under this interpretation, the jet from the nucleus must be deflected through ~20° (projected onto the plane of the sky) by the cloud before continuing on to the northern hot spot (Tingay 1997; Tingay et al. 2002). Using some of our measured quantities, it is possible to make an estimate of the jet speed at the cloud complex, following the calculations of Bicknell et al. (1998) and Kadler et al. (2003). Using the expressions for the jet power in Bicknell et al. (1998), we estimate a jet power, $F_j = 5\times10^{41} - 5\times10^{43}$ ergs s^{-1} (assuming that κ_ν, the ratio of

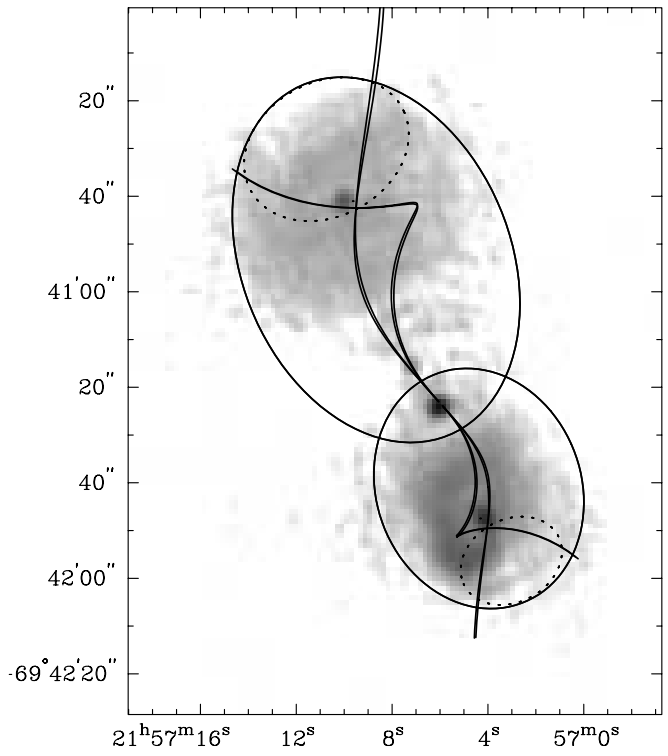

FIG. 15.—Jet precession model for PKS 2153−69 overlaid on a 4.7 GHz radio map (Fosbury et al. 1998). The radio lobes are approximated by spheroids (*solid ellipses*) and the lobe hot spots are assumed to lie on the surface of the spheroids at the intersection of the spheroid surfaces and the cone formed by the precessing jet direction (*dotted ellipses*). Four possible solutions are shown by the curved lines (since there are two possible precession directions and two possible azimuthal positions of the parsec-scale jet that give the same projected position). The model and its parameters are described in § 5.6.

monochromatic power at frequency ν to total jet flux, lies in the range $10^{-11} < \kappa_\nu < 10^{-9}$, and that the radio flux density at 1.4 GHz is half of the total flux density of the entire source at 1.4 GHz, to reflect the power in only the northern jet). This compares to the $\sim 2 \times 10^{42}$ ergs s^{-1} estimated in § 5.1. The jet speed can then be estimated as

$$v_j \sim \frac{0.5 f(M_j,\ \Delta\theta) F_j v_s}{L_{\rm X}}, \qquad (5)$$

where $L_{\rm X}$ is the X-ray luminosity associated with the cloud complex ($L_{\rm X} = 1.1 \times 10^{41}$ ergs s^{-1} between 0.5 and 7 keV), v_s is the shock velocity ($\simeq$430 km s^{-1} from eq. [3]), and $f(M_j, \Delta\theta)$ is described and calculated in Bicknell et al. (1998) for a nonrelativistic jet, depending on the jet Mach number, M_j, and the jet deflection angle, $\Delta\theta$. For PKS 2153−69, taking $\Delta\theta = 20^\circ$ (Tingay et al. 1996) and $f(M_j,\ \Delta\theta) \sim 0.5$, we estimate that $v_j < 0.2c$.

It is interesting to compare these mildly relativistic jet speeds with the estimate made by Tingay et al. (1996) starting from the assumption of a *relativistic* jet at the clouds, resulting in $v_j > 0.9c$. The calculation of Tingay et al. (1996) does not use the X-ray emission as a constraint on the jet energetics (because no suitable observations were available at that point) and considers simple oblique shocks in a relativistic jet.

Other interpretations of S-shaped radio sources include jet bending by the thermal pressure of a hot, gaseous atmosphere (Henriksen et al. 1981) or by the ram pressure of rotating interstellar gas (Wilson & Ulvestad 1982).

6. CONCLUSIONS

In this paper we present the results of *Chandra* and 1.4 GHz LBA observations of the radio galaxy PKS 2153−69 and its environment. Our conclusions are summarized below.

1. The *Chandra* image reveals a roughly spherical halo of hot gas extending out to 30 kpc around PKS 2153−69 with a temperature of $kT = 1.01$ keV, a 0.5–2 keV luminosity of 7×10^{41} ergs s^{-1}, and a total gas mass of $3 \times 10^{10}\ M_\odot$ (the total gravitating mass is likely much larger). Two depressions in the surface brightness of the X-ray halo correspond to the large-scale radio lobes, and assuming that these are cavities inflated by the jet, we infer a total jet power (both sides) of 4×10^{42} ergs s^{-1}.

2. Both the northern and southern lobe hot spots are detected by *Chandra*. In addition, the southern hot spot is detected in the 1.4 GHz VLBI observation, providing the highest linear resolution image of a radio lobe hot spot to date. The northern hot spot is not detected in the VLBI observation.

3. The X-ray spectrum of the nucleus is well described by a power law of photon index $\Gamma = 1.75$ absorbed by the Galactic column, with a 2–10 keV X-ray luminosity of 9×10^{42} ergs s^{-1}. This photon index is typical of a type 1 active galaxy. The 1.4 GHz VLBI image of the nucleus shows a jet on 0.″1 scales along a P.A. of 45°. The absence of a detectable counterjet constrains the jet speed v_j ($\beta_j = v_j/c$) and inclination angle θ to be $\beta_j \cos\theta > 0.37$ on parsec scales.

4. Approximately 10″ northeast of the nucleus, at a position angle intermediate between that of the northern hot spot and the direction of the nuclear jet, X-ray emission is detected from an extranuclear cloud. The X-ray emission from the cloud can be divided into two regions—an unresolved western component associated with a knot of radio emission, and a spatially resolved eastern component associated with highly ionized optical line-emitting clouds. The radio spectrum of the western component is consistent with synchrotron emission, with the optical continuum being predominantly red light scattered from nuclear light impinging on the cloud by large dust grains and the X-ray emission being from a hot thermal plasma. The X-ray emission of the eastern component has a 0.5–2 keV luminosity of 7×10^{40} ergs s^{-1} and is very soft ($\Gamma > 4$ or $kT \simeq 0.2$ keV). The eastern component is probably being photoionized by radiation beamed from the nucleus with the polarized blue optical continuum and soft X-ray emission being beamed radiation from the nucleus scattered into our line of sight by dust in the clouds. The interpretation of this soft X-ray emission as dust-scattered nuclear light is speculative and appears to require that the radio axis of PKS 2153−69 is within several degrees of our line of sight. If correct, this is the first detection of dust-scattered X-rays in an extragalactic object. The 1.4 GHz VLBI observation did not detect compact radio emission from the extranuclear cloud.

5. We account for the progressive increase of P.A. from the northern hot spot to the western region of the extranuclear cloud to the parsec-scale radio jet in terms of a jet precession model in which the particle beam interacts with the western component of the jet/cloud interaction region and the radiation beam interacts with the eastern component. The jet speed is estimated to be $<0.5c$ and the precession rate to be $\simeq 2 \times 10^{-4}$ deg yr^{-1}. The model is consistent with the location of the southern hot spot, which gives the source an overall S-shape. We discuss the alternative possibility of jet deflection.

6. X-ray emission from the nearby radio galaxy MRC 2153−699 is detected in the *Chandra* image.

Our findings are consistent with and complementary to the presentation of the X-ray observations in a paper by Ly et al. (2004) that appeared during the refereeing of our paper.

We thank R. Fosbury for providing electronic copies of his radio maps. This work was supported by NASA through contract NAS8-01129 and grants NAG8-1027 and NAG5-13065, Chandra Fellowship Award PF3-40026 issued by the *Chandra X-Ray Observatory* Center, which is operated by the Smithsonian Astrophysical Observatory for and on behalf of the NASA under contract NAS8-39073, and by a grant from the Research and Development Grants Scheme of the Swinburne University of Technology. The Australia Telescope is funded by the Australian Commonwealth Government for operation as a national facility managed by the CSIRO.

REFERENCES

Arnaud, K. A. 1996, in ASP Conf. Ser. 101, Astronomical Data Analysis Software and Systems V, ed. G. H. Jacoby & J. Barnes (San Francisco: ASP), 17
Bennett, C. L., et al. 2003, ApJS, 148, 1
Bicknell, G. V. 1994, ApJ, 422, 542
Bicknell, G. V., Dopita, M. A., Tsvetanov, Z. I., & Sutherland, R. S. 1998, ApJ, 495, 680
Carilli, C. L., Perley, R. A., Dreher, J. W., & Leahy, J. P. 1991, ApJ, 383, 554
Davis, J. E. 2001, ApJ, 562, 575
De Young, D. S. 2005, in X-Ray and Radio Connections, ed. L. Sjouwerman & K. Dyer (Socorro: NRAO), in press
Dickey, J. M., & Lockman, F. J. 1990, ARA&A, 28, 215
di Serego Alighieri, S., Courvoisier, T. J.-L., Fosbury, R. A. E., Tadhunter, C. N., & Binette, L. 1988, Nature, 334, 591
Draine, B. T. 2003, ApJ, 598, 1017
Draine, B. T., & Tan, J. C. 2003, ApJ, 594, 347
Fosbury, R. A. E., Di Serego Alighieri, S., Courvoisier, T. J.-L., Snijders, M. A. J., Tadhunter, C. N., Walsh, J., & Wilson, W. 1990, in Evolution in Astrophysics: *IUE* Astronomy in the Era of New Space Missions, ed. E. Rolfe (ESA SP-310; Noordwijk: ESA), 513
Fosbury, R. A. E., Morganti, R., Wilson, W., Ekers, R. D., di Serego Alighieri, S., & Tadhunter, C. N. 1998, MNRAS, 296, 701
Fossati, G., Maraschi, L., Celotti, A., Comastri, A., & Ghisellini, G. 1998, MNRAS, 299, 433
Hardcastle, M. J., Worrall, D. M., Kraft, R. P., Forman, W. R., Jones, C., & Murray, S. S. 2003, ApJ, 593, 169
Henriksen, R. N., Vallee, J. P., & Bridle, A. H. 1981, ApJ, 249, 40
Hughes, P. A., Miller, M. A., & Duncan, G. C. 2002, ApJ, 572, 713
Jones, P. A., & McAdam, W. B. 1992, ApJS, 80, 137
Kaastra, J. S. 1992, An X-Ray Spectral Code for Optically Thin Plasmas, Internal SRON-Leiden Rep., updated Ver. 2.0
Kadler, M., Ros, E., Kerp, J., Falcke, H., Zensus, J. A., Pogge, R. W., & Bicknell, G. V. 2003, NewA Rev., 47, 569
Landau, L. D., & Lifshitz, E. M. 1959, Fluid Mechanics (Oxford: Pergamon)
Liedahl, D. A., Osterheld, A. L., & Goldstein, W. H. 1995, ApJ, 438, L115
Ly, C., De Young, D., & Bechtold, J. 2004, AAS/Head Meeting, 8, 04.18
Mewe, R., Gronenschild, E. H. B. M., & van den Oord, G. H. J. 1985, A&AS, 62, 197
Mewe, R., Lemen, J. R., & van den Oord, G. H. J. 1986, A&AS, 65, 511
O'Dea, C. P., de Vries, W. H., Koekemoer, A. M., Baum, S. A., & Mack, J. 2002, in Rev. Mex. AA Ser. Conf. 13, Emission Lines from Jet Flow, ed. W. J. Henry et al. (Mexico, DF: Inst. Astron., UNAM), 196
Perley, R. A., Röser, H., & Meisenheimer, K. 1997, A&A, 328, 12
Sault, R. J., Teuben, P. J., & Wright, M. C. H. 1995, in ASP Conf. Ser. 77, Astronomical Data Analysis Software and Systems IV, ed. R. A. Shaw, H. E. Payne, & J. J. E. Hayes, (San Francsico: ASP), 433
Shepherd, M. C. 1997, in ASP Conf. Ser. 125, Astronomical Data Analysis Software and Systems VI, ed. G. Hunt & H. E. Payne (San Francisco: ASP), 77
Snellen, I. A. G., Mack, K.-H., Schilizzi, R. T., & Tschager, W. 2003, Publ. Astron. Soc. Australia, 20, 38
Tadhunter, C. N., Fosbury, R. A. E., Binette, L., Danziger, I. J., & Robinson, A. 1987, Nature, 325, 504
Tadhunter, C. N., Fosbury, R. A. E., di Serego Alighieri, S., Bland, J., Danziger, I. J., Goss, W. M., McAdam, W. B., & Snijders, M. A. J. 1988, MNRAS, 235, 403
Tingay, S. J. 1997, A&A, 327, 550
Tingay, S. J., et al. 1996, AJ, 111, 718
———. 2002, ApJS, 141, 311
Villar-Martín, M., De Young, D., Alonso-Herrero, A., Allen, M., & Binette, L. 2001, MNRAS, 328, 848
Wietfeldt, R. D., Baer, D., Cannon, W. H., Feil, G., Jakovina, R., Leone, P., Newby, P. S., & Tan, H. 1996, IEEE Trans. Instrum. Meas., 45(6), 923
Wilson, A. S., & Ulvestad, J. S. 1982, ApJ, 263, 576
Wilson, A. S., Young, A. J., & Shopbell, P. L. 2001, ApJ, 547, 740
Wilson, W., Roberts, P., & Davies, E. 1996, Proc. 4th Asia-Pacific Telescope Workshop, ed. E. A. King (Sydney: ATNF/CSIRO), 16